Asian Journal of Chemistry; Vol. 38, No. 3 (2026), 747-754
ASIAN JOURNAL OF CHEMISTRY
https://doi.org/10.14233/ajchem.2026.35315

Hydrothermal Synthesis, Characterization and Biocompatibility Study of Thermally Modified Hydroxyapatite Nanoparticles

AMOL B. CHAVAN[1,2], SANJAYKUMAR S. GAWADE[3,*] and PARVEJHA S. MALDAR[4]

[1]Department of Mechatronics Engineering, Kasegaon Education Society's Rajarambapu Institute of Technology (Affiliated to Shivaji University, Kolhapur), Sakharale-415414, India
[2]Department of Mechanical Engineering, Department of Technology, Shivaji University, Kolhapur-416004, India
[3]Department of Mechanical Engineering, Kasegaon Education Society's Rajarambapu Institute of Technology (Affiliated to Shivaji University, Kolhapur), Sakharale-415414, India
[4]Department of Sciences and Humanities, Kasegaon Education Society's Rajarambapu Institute of Technology (Affiliated to Shivaji University, Kolhapur), Sakharale-415414, India

*Corresponding author: E-mail: sanjaykumar.gawade@ritindia.edu

Received: 23 November 2025 *Accepted*: 27 January 2026 *Published online*: 6 March 2026 AJC-22294

The hydrothermal synthesis of hydroxyapatite nanoparticles (HANPs) followed by comprehensive characterization using XRD, SEM, TEM, XPS, FTIR, Raman spectroscopy, and cytotoxicity analysis, enabling systematic evaluation of the effects of hydrothermal processing and post-synthesis heat treatment on the structural properties and biological response of HANPs were carried out. In this work, calcium nitrate tetrahydrate, ammonium dihydrogen phosphate, and ammonia solution were used as precursors. The synthesized HANPs were subsequently heat-treated at 200 ºC, 300 ºC and 400 ºC, and the treated samples were evaluated for phase composition, structural morphology and cytotoxicity. The synthesized HANPs exhibited a hexagonal crystal structure with an average crystallite size of 24.87 nm and the cytotoxicity results confirmed their biocompatibility. These structural and biological characteristics indicate that HANPs prepared through this method are promising biomaterials for potential biomedical applications, while the synthesis approach remains simple and cost-effective.

Keywords: Hydroxyapatite, Hydrothermal method, Nanoparticles, Biomaterial, Cytotoxicity.

INTRODUCTION

Hydroxyapatite (HA) [$Ca_5(PO_4)_3(OH)$ or $Ca_{10}(PO_4)_6(OH)_2$] represents the highly stable form of calcium phosphate in a physiological environment [1]. Besides its relevance in many commercial utilities, it has numerous biomedical applications, such as dentistry and orthopedics [2]. Due to its diverse biomedical applications, biocompatibility, biodegradability, osteoconductivity and osteoinductivity, which support bone formation and remodelling, particularly in orthopedic treatments many researchers have extensively studied [3-9]. The compositional similarity of hydroxyapatite to human bone is a significant factor in this growing interest. Moreover, HA can chemically interact with natural bone due to its compositional similarity. In stoichiometric HA, the calcium-to-phosphorus (Ca:P) ratio is 1.67, although achieving this exact ratio is often challenging, leading to the formation of non-stoichiometric phases such as oxy-HA, calcium-deficient HA and carbonated HA. Despite having a density of approximately 3.16 g cm^{-3}, the brittle nature of HA limits its use in load-bearing applications. Consequently, it is commonly employed as a coating material for biomedical implants to enhance surface bioactivity and bone integration [10-13].

Several synthesis methods have been explored for obtain hydroxyapatite nanoparticles (HANPs), broadly classified into dry methods, wet methods and high-temperature processes. Among these, wet methods include techniques such as chemical precipitation, emulsion, hydrolysis, sol-gel, sonochemical and hydrothermal synthesis [14-23]. Among these, the hydrothermal technique is the most often utilised approach for synthesising HANPs. The reaction is carried out in an autoclave at elevated temperature and pressure, this facilitates the formation of highly crystalline HANPs [24].

The hydrothermal method is widely used for synthesising hydroxyapatite nanoparticles (HANPs) at the nanometer scale. The process begins with the pre-paration of suitable precursors containing the core elements of HA, calcium (Ca) and phosphorus (P). Common calcium sources include calcium nitrate, calcium chloride and calcium hydroxide, while phosphorus is typically supplied by phosp-horic acid or ammonium phosphate [21-28]. In current inves-tigation, calcium nitrate tetrahydrate has been utilised as a source of Ca and ammonium phosphate monobasic as a P source. The obtained HANPs were subjected to investigation of physio-chemical characteristics and the biocompatibility analysis were also reported.

EXPERIMENTAL

Preparation of hydroxyapatite nanoparticles (HANPs): All the reagents used were of analytical grade and procured from Sigma-Aldrich, USA. In brief, 0.085 M calcium pre-cursor solution ($Ca(NO_3)_2 \cdot 4H_2O$) was prepared in deionized water, followed by dropwise addition of 2.355 M NH_4OH under continuous stirring. Separately, 0.051 M $NH_4H_2PO_4$ solution was prepared and gradually added to the calcium containing solution while stirring for 30 min until the pH reached approximately 12. The resulting mixture was trans-ferred into a Teflon-lined autoclave and subjected to hydro-thermal treatment at 150 ºC for 24 h. After cooling, the pro-duct was filtered, washed with ethanol and deionized water, and dried at 60 ºC for 6 h. The dried material was then ground into a fine powder and calcined at 300 ºC for 3 h to obtain HANPs.

Characterisation: The obtained HANPs were analysed for the phase composition, structural morphology and biocom-patibility. The phase composition was characterised *via* X-ray diffraction (XRD) (AXS-D8-Advance, Bruker Ltd.), empl-oying Cu*K*α radiation (λ = 1.54 Å). All the measurements were executed over a 2θ span of 10º to 90º with an increment of 0.002º. The crystallite size (D) was calculated following the Scherrer equation (eqn. 1):

$$D = \frac{0.9\lambda}{\beta \cos\theta} \quad (1)$$

here λ represents the wavelength of electromagnetic radiation (0.154 nm); β is the full width at half-maximum of the peak being analysed and θ corresponds to the Bragg's angle of the highest intensity diffracted peak.

Scanning electron microscope (SEM, JEOL, JSM IT-200) imaging of the microstructure was executed in high vacuum conditions at 20 kV of accelerating voltage. The information on the crystal orientation of HANPs was obtained by transmi-ssion electron microscope (TEM, JEM 2100 PLUS, JEOL Asia PTE Ltd). An acceleration voltage of 200 kV was used for the acquisition of TEM micrographs. X-ray photoelectron spectroscopy (XPS) analysis of HANPs was performed on XPS, JPS 9030, JEOL Asia PTE Ltd. The test was executed under high vacuum conditions, ranging from 10^{-6} to 10^{-7} Pa. Raman spectrum in the 100 to 4000 cm^{-1} range was recorded using Renishaw INVIA 0120-02, UK. The diode laser source (λ = 532 nm) with spectral resolution 0.5 cm^{-1} was used for analysis. The FTIR analysis (Alpha, Bruker) was carried out in the 4000-400 cm^{-1} region to identified the functional groups and characterised the covalent bonding information of HANPs.

Cytotoxicity studies: The MTT assay was employed to determine the cytotoxicity of the HANPs sample using L929 (normal fibroblast) cells. The L929 cell suspension media utilised in the analysis contained DMEM with high glucose (HiMedia), FBS (Gibco) and antibiotic-antimycotic 100X solution (Thermo-Fisher Scientific). The cell suspension was introduced consistently at a density of 10^4 cells per well in triplicate into a 96-well plate and maintained for 24 h in humidified conditions with 5% CO_2 at 37 ºC. The cells were exposed to HANPs and the standard (fluorouracil, 5-FU) at five different concentrations ranging from 20 to 100 μg/mL. Control wells, consisting of cells incubated with 0.2% DMSO in PBS (phosphate-buffered saline), were served to establish baseline cell viability. The culture medium was then removed after treatment and 20 μL of MTT reagent (5 mg/mL in PBS) was subsequently added. The plates went through an addi-tional 4 h incubation at 37 ºC in a CO_2 incubator to enable the formation of formazan crystals. The medium was then dis-carded, followed by the addition of 200 μL of DMSO to solubilize the formazan crystals. Incubation of the plates was continued at 37 ºC in dark for an additional 10 min. The absorbance at 550 nm was captured using a microplate reader and the resulting data was used to evaluate cell viability by the absorbance differences between treated samples and the control.

RESULTS AND DISCUSSION

XRD studies: The crystalline structure and phase charac-teristics of HANPs [$Ca_5(PO_4)_3(OH)$], before and after calci-nation, were evaluated with the help of XRD technique. The XRD diffractograms of HANPs with and without calcination are illustrated in Fig. 1. The signals on XRD patterns of HANPs show the hexagonal crystal system with the space group $P6_3/m$. Further, it revealed the polycrystalline nature of HANPs with the preferred orientation along the (121) plane.

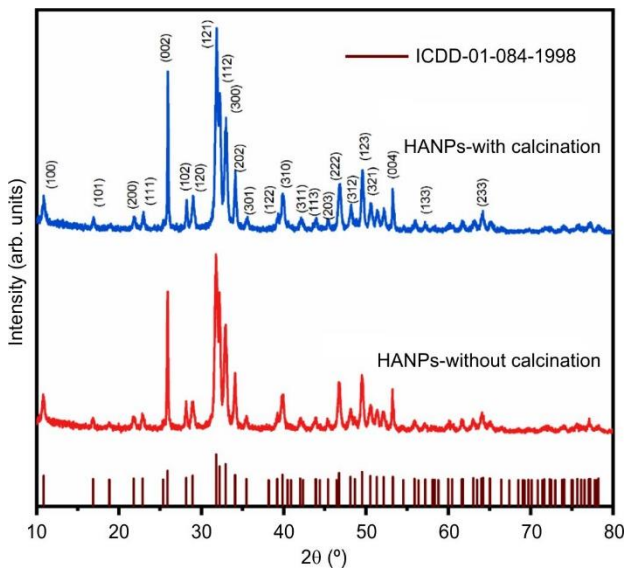

Fig. 1. XRD patterns of HANPs, with and without calcination

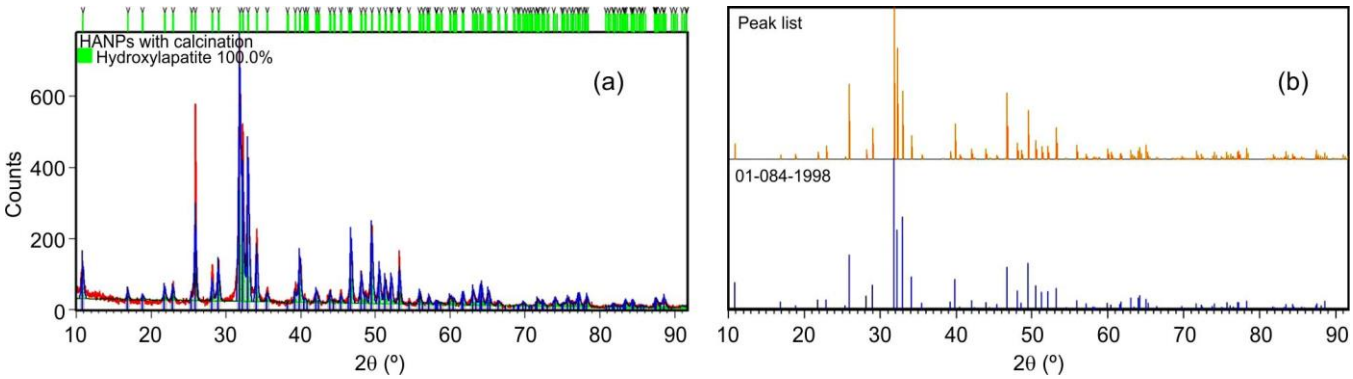

Fig. 2. (a) Rietveld refinement of HANPs and (b) Stick pattern of calcinated HANPs

It can also be observed that the HANPs without calcination show low crystallinity as compared with the calcinated HANPs. The most prominent signals for HANPs are the peaks at 31.80º and 32.90º, attributed to the crystallisation planes (121) and (300), respectively. The index Miller peaks (002), (202), (310) and (222) further extended the concurrence of the results and consistent with previous reports [29,30]. Furthermore, the crystallite size of 27.18 nm was obtained using the Scherrer equation (eqn. 1). The obtained patterns are also in good consistency with the characteristic patterns of pure-HA as in the reference ICDD-01-084-1998 (Fig. 2). It is obviously observed that calcination of HANPs increased their crystallinity, as evidenced by sharper and more intense XRD peaks compared to uncalcined sample, consistent with previous reports [31-34]. Therefore, calcined HANPs were used for further analysis.

Rietveld refinement generated lattice parameters of hydrothermally synthesised HANPs as a = b = 9.41 Å, c = 6.88 Å, $\alpha = \beta = 90^{o}$ and $\gamma = 120^{o}$. These parameters corroborated the hexagonal phase of HANPs [10]. Fig. 3 depicts the crystal structure of HANPs.

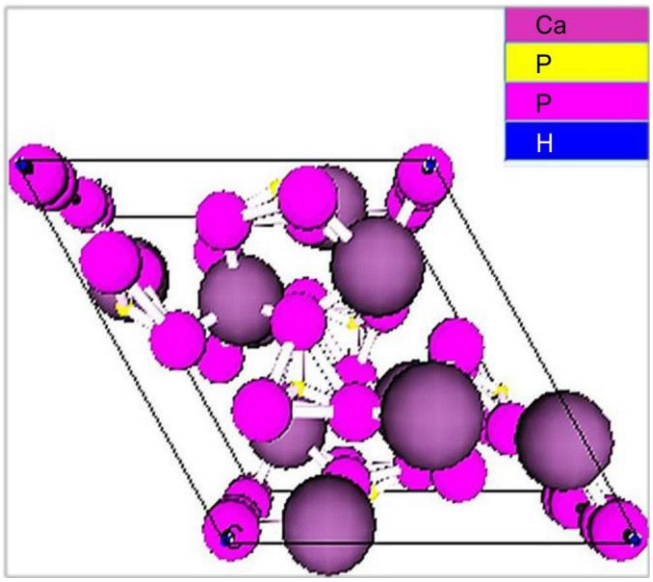

Fig. 3. Crystal structure of calcinated HANPs

Surface morphology: The images obtained from the SEM of calcinated HANPs are displayed in Fig. 4a-b. These images mirrored a high degree of agglomeration in the HANPs. The spherical particles of HANPs exhibiting clumped distributions are visible, which is potential indicator of Ostwald ripening contributing to the observed agglomeration [35]. Fig. 4c shows the EDX spectrum of hydrothermally synthesised HANPs. The spectrum confirms the presence of Ca, P and O, with atomic percentages of 19.24, 12.00 and 68.75, respectively, yielding a Ca/P ratio of 1.60, which is close to the stoichiometric value.

TEM image (Fig. 5a) revealed a cylindrical morphology of the nanoparticles, with an average particle diameter of approximately 28.1 nm, indicating that the size and morphology of the synthesized HANPs are comparable to those of bone hydroxyapatite [34]. Fig. 5b shows the elemental mapping of different constituent elements of HANPs and it is inferred that the distribution of elements such as Ca, O and P is uniform. This characteristic, with its abundance of active sites, is expected to enhance the efficacy of the HANPs in various applications.

XPS studies: The survey and narrow scan spectra of the HANPs sample are displayed in Figs. 6 and 7, respectively. Table-1 shows the elements, their binding energy and respective XPS narrow scan analysis assignments. Fig. 6 shows characteristic XPS peaks corresponding to C 1s, O 1s, P 2p, Ca 2p, Ca 3p, Ca 3s and Ca LMM, confirming the presence of the primary constituent elements of hydroxyapatite, namely Ca, P and O [36]. The C 1s peak at approximately 285 eV is commonly attributed to adventitious carbon contamination, a typical feature in XPS spectra [36], thereby supporting the identification of HA in the sample.

Fig. 7 presents the high-resolution XPS spectra used to examine the chemical states of Ca, P, O and C in the sample. The Ca 2p spectrum (Fig. 7a) shows peaks at 348.37 eV (Ca $2p_{3/2}$) and 351.85 eV (Ca $2p_{1/2}$), with a splitting of 3.48 eV, confirming the +2 oxidation state of calcium [36-40]. The P 2p spectrum (Fig. 7b) displays a peak at 134.30 eV, corresponding to phosphate (PO_4^{3-}) and indicating P^{5+} in hydroxyapatite [36,39]. The O 1s spectrum (Fig. 7c) shows a peak centered at ≈532 eV, attributed to oxygen in phosphate and hydroxyl groups [37-39,41]. The C 1s spectrum (Fig. 7d) exhibits a peak at 285 eV, typically associated with extraneous carbon used as a charge reference [37,39,42]. Thus, the binding-energy values of Ca 2p, P 2p, and O 1s are consistent with stoichiometric hydroxyapatite, confirming the formation of a well-defined HA phase.

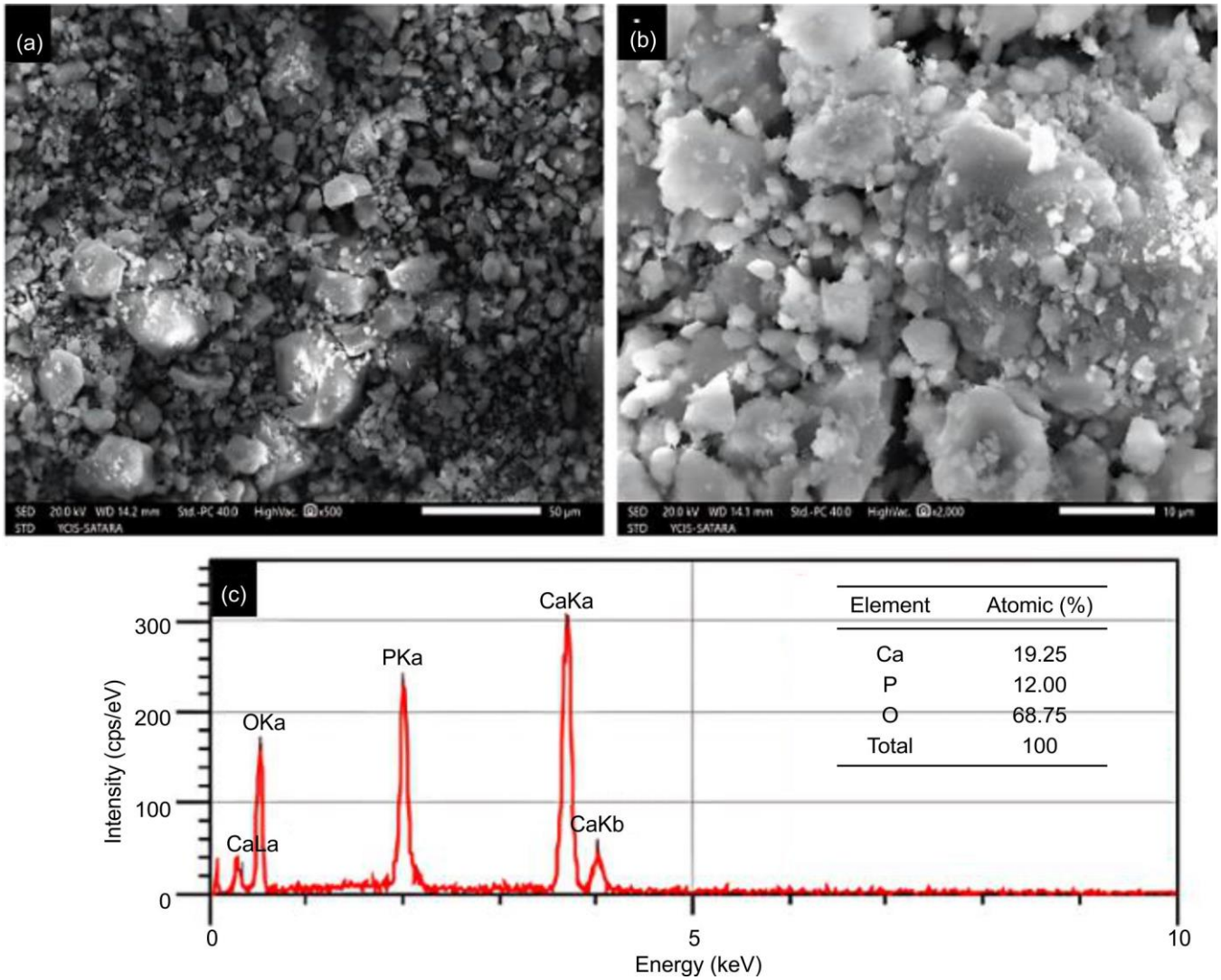

Fig. 4. (a) SEM images of calcinated HANPs at 500x, (b) SEM images of calcinated HANPs at 2000x, (c) EDS spectrum of calcinated HANPs

TABLE-1
ELEMENTS, BINDING ENERGY AND ASSIGNMENTS OF XPS NARROW SCAN ANALYSIS OF CALCINATED HANPs

Element	Narrow scan	Binding energy (eV)	Assignment	Ref.
Ca	Ca 2p	Ca $2p_{3/2}$-348.37 eV	+2 oxidation state of Ca	[36]
		Ca $2p_{1/2}$-351.85 eV		[37]
P	P 2p	134.30	+5 oxidation of phosphorus	[36,39]
O	O 1s	532	Presence of oxygen in phosphate (PO_4^{3-}) and hydroxyl (OH^-) group	[37,39,41]
C	C 1s	285	Adventitious carbon indicating C-C bonds	[37,42]

Raman spectral studies: Raman spectrum of hydrothermally synthesised HANPs is shown in Fig. 8. A high-intensity band at 960 cm^{-1} correspond to the symmetric stretching mode (ν_1) of phosphate, which is a distinctive peak of HA [12,43-47]. The asymmetric stretching mode (ν_3) of PO_4^{3-} was detected in the 1095-1020 cm^{-1} range, whereas the symmetric bending mode (ν_2) of PO_4^{3-} ion was appeared in the 490-400 cm^{-1} region [12,44]. On the other hand, the asymmetric bending mode (ν_4) of PO_4^{3-} and its components was observed between 625 and 570 cm^{-1}. Furthermore, the OH^- stretching vibrations appeared weak at 3572 cm^{-1} [43,48] (Table-2). Thus, the peaks stretching vibrations of the PO_4^{3-} ion and OH^- ion affirm the formation of HANPs.

TABLE-2
RAMAN BAND POSITIONS AND VIBRATIONAL ASSIGNMENT OF CALCINATED HANPs

Wavenumber (cm^{-1})	Band assignment
962	ν_1 Symmetric stretching mode of PO_4^{3-}
434	ν_2 (PO_4^{3-} internal modes)
598	ν_4 (PO_4^{3-} internal modes)
1051	ν_3 (PO_4^{3-} internal modes)
3572	OH stretch

FTIR spectral studies: Fig. 9 shows the FTIR spectrum of HANPs calcinated at 300 ºC for 3 h. The inset of the figure further illustrates the band assignment of the HANPs

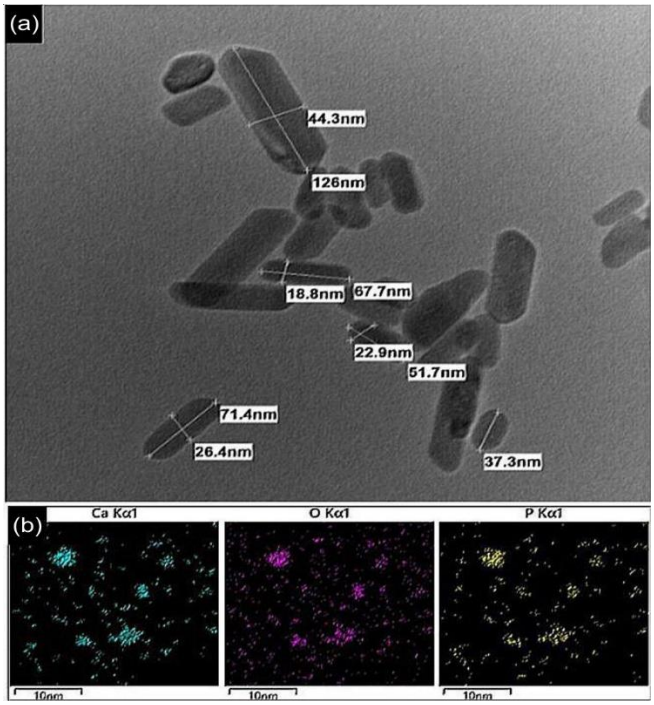

Fig. 5. (a) TEM image of calcinated HANPs, (b) Elemental mapping of the constituent elements of HANPs

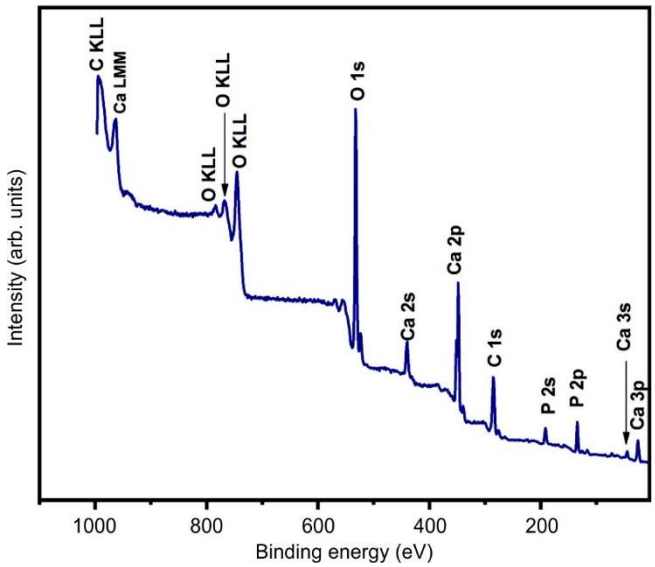

Fig. 6. Survey scan spectrum of HANPs

over the 1200-400 cm^{-1} region. The O–H stretching band at 3572 cm^{-1} is characteristic of structural hydroxyl groups in hydroxyapatite (HA), confirming their presence in the crystalline HA lattice [49,50]. The PO_4^{3-} vibrational bands obser-

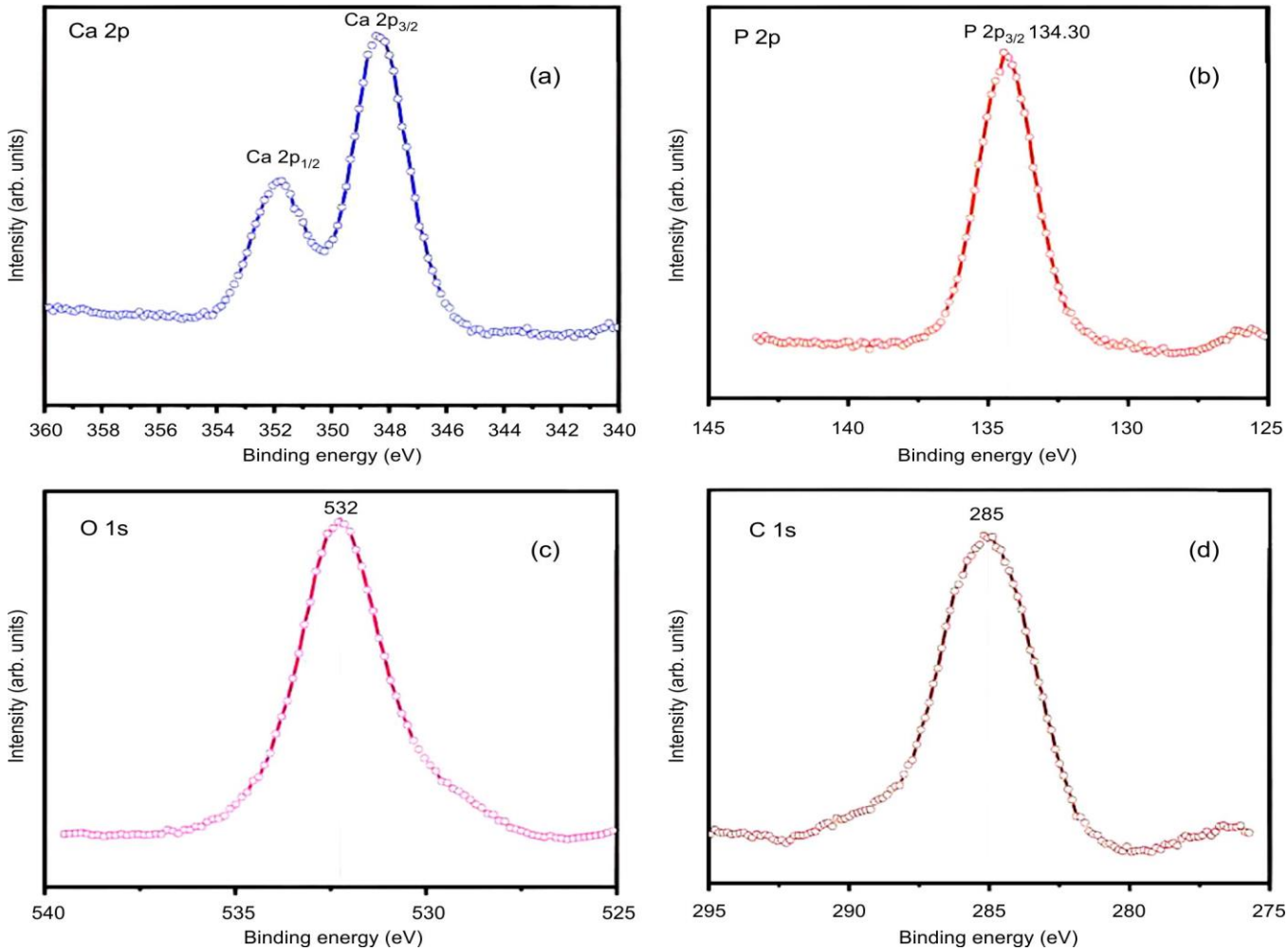

Fig. 7. Narrow scan spectrum of (a) Ca 2p (b) P 2p (c) O 1s (d) C 1s

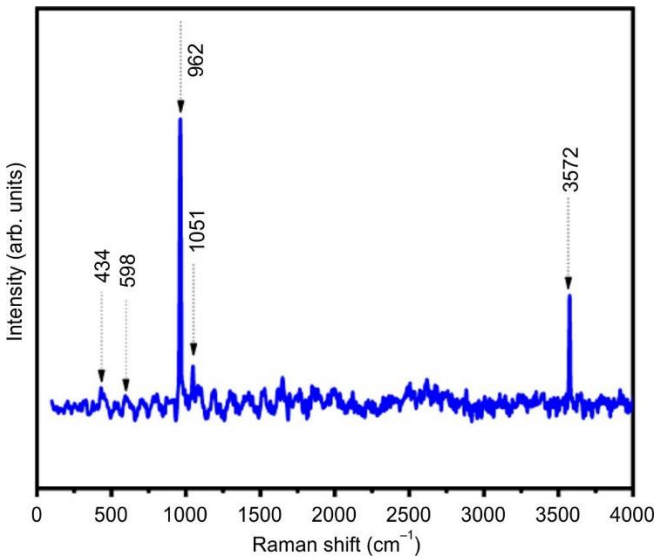

Fig. 8. Raman spectrum of hydrothermally synthesised HANPs

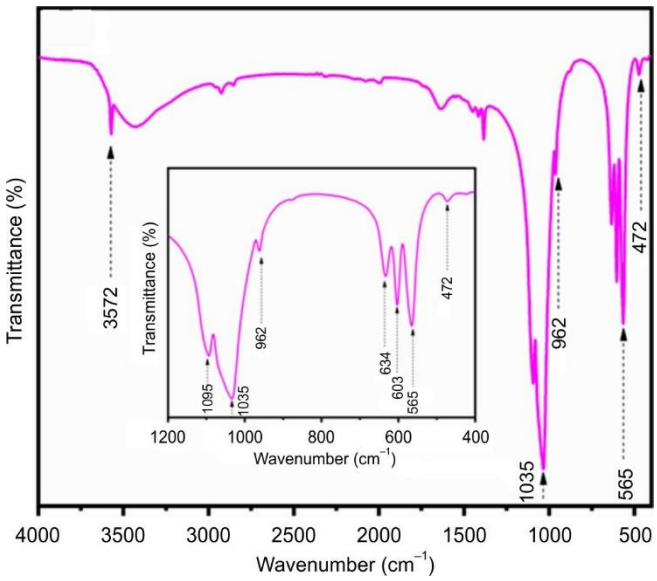

Fig. 9. FTIR spectrum of calcinated HANPs

ved at 1035 cm^{-1} (ν_3 asymmetric stretching), 962 cm^{-1} (ν_1 symmetric stretching), and 603 and 565 cm^{-1} (ν_4 bending modes) represent the principal stretching and bending vibrations of PO_4^{3-} groups, thereby confirming the presence of PO_4^{3-} units in the HANPs sample. The absence of significant CO_3^{2-} bands (~1420 cm^{-1}, 870 cm^{-1}) proposes low or no CO_3^{2-} substitution, meaning the HA is not significantly carbonated [51]. Thus, the FTIR spectrum strongly suggests HA as the primary phase, with good crystallinity.

Cytotoxicity studies: The MTT assay method was employed to evaluate the *in vitro* cytotoxicity of HANPs [52,53]. The microscopic images, observed with the inverted phase contrast microscope of L929 fibroblast cells cultured along with control, standard and HANPs in a 96-well plate for 24 h are shown in Fig. 10. In Fig. 11, the graphical representation depicts the viability of L929 fibroblast cells after exposure to the varying HANPs dosages (20, 40, 60, 80, 100 µg/mL) for 24 h. The results demonstrated a dose-dependent increase in cytotoxicity, wherein higher HANP concentrations caused a gradual rise in cell inhibition and a corresponding drop in cell viability [54,55].

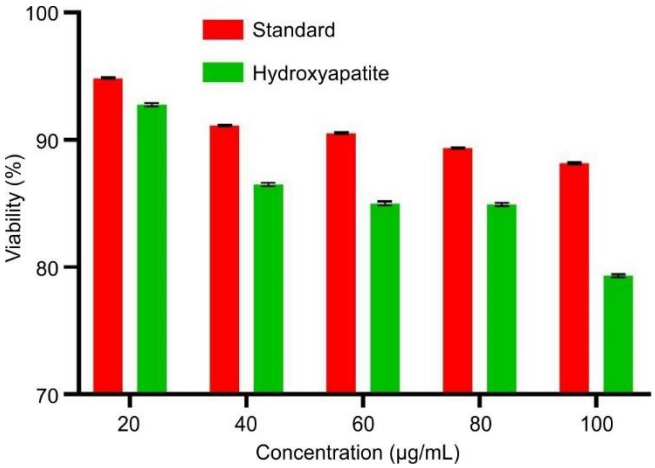

Fig. 11. Viability data of L929 fibroblast cells after exposure to different concentrations of HANPs for 24 h

Materials demonstrating less than 30% cell inhibition are generally considered cytocompatible according to ISO 10993-5 [56,57]. Across the tested concentration range, the HANPs showed acceptable variation in inhibition against the normal fibroblast cell line, with cell viability consistently above 70%, indicating the acceptable cytocompatibility under the studied conditions.

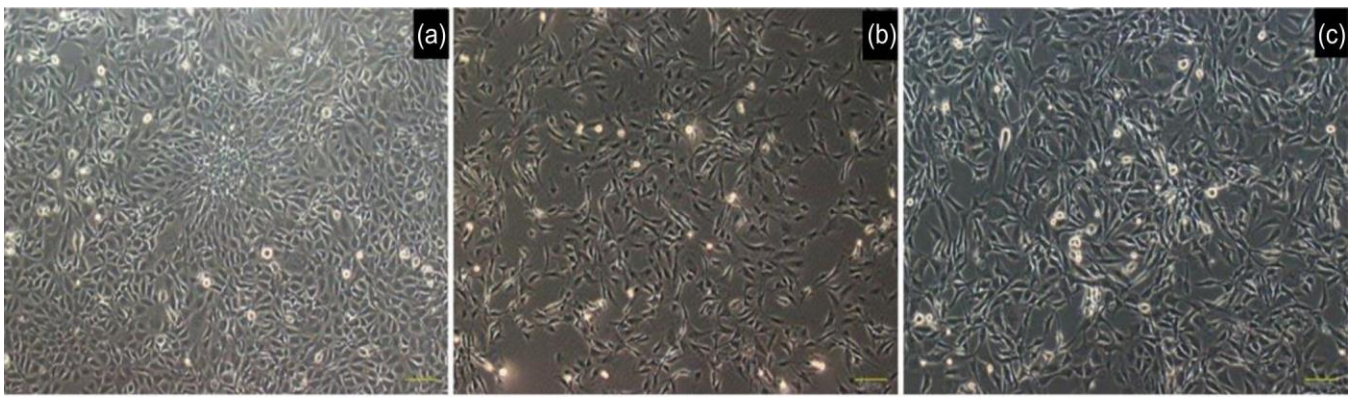

Fig. 10. Microscopic images of L929 fibroblast cells cultured in 96-well plate (a) control, (b) standard and (c) HANPs

Conclusion

In this study, hydroxyapatite nanoparticles (HANPs) were successfully synthesised using the hydrothermal method and characterised. The XRD analysis revealed the polycrystalline nature of HANPs with phase purity. SEM and TEM analysis demonstrated that the HANPs have well-defined morphology. The cylindrical morphology of HANPs, with an average diameter of 28.1 nm, gives a high surface-to-volume ratio. XPS further substantiated the chemical composition, ensuring the key elements in the expected oxidation states are present. The binding energies of P 2p, O 1s and Ca 2p closely correspond to those of stoichiometric HA, confirming the formation of a well-structured HA phase. FTIR and Raman analyses confirmed the featured functional groups and vibrational modes of HA, reinforcing the structural integrity of HANPs. The biological evaluation through cytotoxicity assessment using L929 fibroblast cells and the MTT assay proved that the grown HANPs are non-toxic. Thus, based on these resi;ts, the structural and biological properties of HANPs support medical applications, while future studies may focus on *in vivo* evaluation and functionalization for clinical use.

ACKNOWLEDGEMENTS

This research was financed by Seed Funding Scheme, R & D Cell, Rajarambapu Institute of Technology, Sakharale. The authors acknowledge Common Facility Center, Shivaji University and Yashavantrao Chavan Institute of Science, Satara for prodiving the analysis facilities.

CONFLICT OF INTEREST

The authors declare that there is no conflict of interests regarding the publication of this article.

DECLARATION OF AI-ASSISTED TECHNOLOGIES

During the preparation of this manuscript, the authors used an AI-assisted tool(s) to improve the language. The authors reviewed and edited the content and take full responsibility for the published work.

REFERENCES

1. X. Lin, K. de Groot, D. Wang, Q. Hu, D. Wismeijer and Y. Liu, *Open Biomed. Eng. J.*, **9**, 56 (2015); https://doi.org/10.2174/1874120701509010056
2. R. Narayanan, S.K. Seshadri, T.Y. Kwon and K.H. Kim, *J. Biomed. Mater. Res. B Appl. Biomater.*, **85**, 279 (2008); https://doi.org/10.1002/jbm.b.30932
3. M. Šupová, *Ceram. Int.*, **41**, 9203 (2015); https://doi.org/10.1016/j.ceramint.2015.03.316
4. S.V. Dorozhkin, *Materials*, **2**, 399 (2009); https://doi.org/10.3390/ma2020399
5. R.Z. LeGeros, *Chem. Rev.*, **108**, 4742 (2008); https://doi.org/10.1021/cr800427g
6. E. Fiume, G. Magnaterra, A. Rahdar, E. Verné and F. Baino, *Ceramics*, **4**, 542 (2021); https://doi.org/10.3390/ceramics4040039
7. H. Zhou and J. Lee, *Acta Biomater.*, **7**, 2769 (2011); https://doi.org/10.1016/j.actbio.2011.03.019
8. W. Cao and L.L. Hench, *Ceram. Int.*, **22**, 493 (1996); https://doi.org/10.1016/0272-8842(95)00126-3
9. T. Albrektsson and C. Johansson, *Eur. Spine J.*, **10**, S96 (2001); https://doi.org/10.1007/s005860100282
10. W.S.W. Harun, R.I.M. Asri, J. Alias, F.H. Zulkifli, K. Kadirgama, S.A.C. Ghani and J.H.M. Shariffuddin, *Ceram. Int.*, **44**, 1250 (2018); https://doi.org/10.1016/j.ceramint.2017.10.162
11. A.B. Chavan, S.S. Gawade and A.P. Bhosale, *Mater. Today Proc.*, **72**, 1361 (2023); https://doi.org/10.1016/j.matpr.2022.09.331
12. S. Koutsopoulos, *J. Biomed. Mater. Res.*, **62**, 600 (2002); https://doi.org/10.1002/jbm.10280
13. R. Chakraborty, S. Sengupta, P. Saha, K. Das and S. Das, *Mater. Sci. Eng. C*, **69**, 875 (2016); https://doi.org/10.1016/j.msec.2016.07.044
14. T. Ikoma, A. Yamazaki, S. Nakamura and M. Akao, *J. Solid State Chem.*, **144**, 272 (1999); https://doi.org/10.1006/jssc.1998.8120
15. H.C. Shum, A. Bandyopadhyay, S. Bose and D.A. Weitz, *Chem. Mater.*, **21**, 5548 (2009); https://doi.org/10.1021/cm9028935
16. W. Zhou, M. Wang, W. Cheung, B. Guo and D. Jia, *J. Mater. Sci. Mater. Med.*, **19**, 103 (2008); https://doi.org/10.1007/s10856-007-3156-9
17. A. Ethirajan, U. Ziener, A. Chuvilin, U. Kaiser, H. Cölfen and K. Landfester, *Adv. Funct. Mater.*, **18**, 2221 (2008); https://doi.org/10.1002/adfm.200800048
18. C. Durucan and P.W. Brown, *J. Mater. Sci. Mater. Med.*, **11**, 365 (2000); https://doi.org/10.1023/A:1008934024440
19. S. Nakamura, T. Isobe and M. Senna, *J. Nanopart. Res.*, **3**, 57 (2001); https://doi.org/10.1023/A:1011407814795
20. A.F. Solano-Arguedas, N. Ortiz and M.L. Montero, *J. Nanopart. Res.*, **27**, 85 (2025); https://doi.org/10.1007/s11051-025-06249-7
21. X. Guo, P. Xiao, J. Liu and Z. Shen, *J. Am. Ceram. Soc.*, **88**, 1026 (2005); https://doi.org/10.1111/j.1551-2916.2005.00198.x
22. K. Zhu, K. Yanagisawa, A. Onda, K. Kajiyoshi and J. Qiu, *Mater. Chem. Phys.*, **113**, 239 (2009); https://doi.org/10.1016/j.matchemphys.2008.07.049
23. N.A.S. Mohd Pu'ad, R.H. Abdul Haq, H. Mohd Noh, H.Z. Abdullah, M.I. Idris and T.C. Lee, *Mater. Today Proc.*, **29**, 233 (2020); https://doi.org/10.1016/j.matpr.2020.05.536
24. J. Liu, X. Ye, H. Wang, M. Zhu, B. Wang and H. Yan, *Ceram. Int.*, **29**, 629 (2003); https://doi.org/10.1016/S0272-8842(02)00210-9
25. H.S. Liu, T.S. Chin, L.S. Lai, S.Y. Chiu, K.H. Chung, C.S. Chang and M.T. Lui, *Ceram. Int.*, **23**, 19 (1997); https://doi.org/10.1016/0272-8842(95)00135-2
26. G. Zhang, J. Chen, S. Yang, Q. Yu, Z. Wang and Q. Zhang, *Mater. Lett.*, **65**, 572 (2011); https://doi.org/10.1016/j.matlet.2010.10.078
27. Y. Wang, S. Zhang, K. Wei, N. Zhao, J. Chen and X. Wang, *Mater. Lett.*, **60**, 1484 (2006); https://doi.org/10.1016/j.matlet.2005.11.053
28. P. Feng, R. Zhao, L. Yang, S. Chen, D. Wang, H. Pan and C. Shuai, *Ceram. Int.*, **48**, 33682 (2022); https://doi.org/10.1016/j.ceramint.2022.07.314
29. D. Anandan and A.K. Jaiswal, *Ceram. Int.*, **44**, 9401 (2018); https://doi.org/10.1016/j.ceramint.2018.02.156
30. Y. Han, X. Wang and S. Li, *J. Nanopart. Res.*, **11**, 1235 (2009); https://doi.org/10.1007/s11051-008-9507-8
31. H. Yu, Y. Zhu and B.Q. Lu, *Ceram. Int.*, **44**, 12352 (2018); https://doi.org/10.1016/j.ceramint.2018.04.022
32. J. Chen, Z. Wen, S. Zhong, Z. Wang, J. Wu and Q. Zhang, *Mater. Des.*, **87**, 445 (2015); https://doi.org/10.1016/j.matdes.2015.08.056
33. S.J. Kalita and S. Verma, *Mater. Sci. Eng. C*, **30**, 295 (2010); https://doi.org/10.1016/j.msec.2009.11.007
34. M.A.M. Castro, T.O. Portela, G.S. Correa, M.M. Oliveira, J.H.G. Rangel, S.F. Rodrigues and J.M.R. Mercury, *Bol. Soc. Esp. Ceram. Vidr.*, **61**, 35 (2022); https://doi.org/10.1016/j.bsecv.2020.06.003
35. M.P. Ferraz, F.J. Monteiro and C.M. Manuel, *J. Appl. Biomater. Biomech.*, **2**, 74 (2004).
36. W.J. Landis and J.R. Martin, *J. Vac. Sci. Technol. A*, **2**, 1108 (1984); https://doi.org/10.1116/1.572680

37. T.T. Eighmy, A.E. Kinner, E.L. Shaw, J.D. Eusden Jr. and C.A. Francis, *Surf. Sci. Spectra*, **6**, 193 (1999); https://doi.org/10.1116/1.1247925
38. G.N. Raikar, J.L. Ong and L.C. Lucas, *Surf. Sci. Spectra*, **4**, 9 (1996); https://doi.org/10.1116/1.1247808
39. C.C.M. Negrila, V. Predoi, S.L. Iconaru and D. Predoi, *Molecules*, **23**, 2986 (2018); https://doi.org/10.3390/molecules23112986
40. S. Zhou, J. Ren, L. Wang, L. Liu and C. Deng, *Mater. Adv.*, **4**, 2147 (2023); https://doi.org/10.1039/D3MA00046J
41. M.P. Casaletto, S. Kaciulis, G. Mattogno, A. Mezzi, L. Ambrosio and F. Branda, *Surf. Interface Anal.*, **34**, 45 (2002); https://doi.org/10.1002/sia.1249
42. J.M. Moulder, W.F. Stickle, P.E. Sobol and K.D. Bomben, Handbook of X-ray Photoelectron Spectroscopy, Physical Electronics Inc. (1992).
43. D.G.A. Nelson and B.E. Williamson, *Aust. J. Chem.*, **35**, 715 (1982); https://doi.org/10.1071/CH9820715
44. G. Penel, G. Leroy, C. Rey and E. Bres, *Calcif. Tissue Int.*, **63**, 475 (1998); https://doi.org/10.1007/s002239900561
45. H. Akazawa, *Ceram. Int.*, **48**, 624 (2022); https://doi.org/10.1016/j.ceramint.2021.09.141
46. S. Gamsjaeger, B. Hofstetter, N. Fratzl-Zelman, P. Roschger, A. Roschger, P. Fratzl, W. Brozek, A. Masic, B.M. Misof, F.H. Glorieux, K. Klaushofer, F. Rauch and E.P. Paschalis, *Bone*, **69**, 89 (2014); https://doi.org/10.1016/j.bone.2014.09.012
47. A.M. Sofronia, R. Baies, E.M. Anghel, C.A. Marinescu and S. Tanasescu, *Mater. Sci. Eng. C*, **43**, 153 (2014); https://doi.org/10.1016/j.msec.2014.07.023
48. D. Yamini, G.D. Venkatasubbu, V. Ramakrishnan and J. Kumar, *Spectrochim. Acta A Mol. Biomol. Spectrosc.*, **117**, 299 (2014); https://doi.org/10.1016/j.saa.2013.07.064
49. B.O. Fowler, *Inorg. Chem.*, **13**, 194 (1974); https://doi.org/10.1021/ic50131a039
50. W.H. Sutton, *Am. Ceram. Soc. Bull.*, **68**, 376 (1989).
51. S. Guang, F. Ke and Y. Shen, *J. Mater. Sci. Technol.*, **31**, 852 (2015); https://doi.org/10.1016/j.jmst.2014.12.013
52. S.H. Inayat-Hussain, N.F. Rajab, H. Roslie, A.A. Hussin, A.M. Ali and B.O. Annuar, *Med. J. Malaysia*, **59(Suppl B)**, 176 (2004).
53. M. Alcaide, M.C. Serrano, R. Pagani, S. Sánchez-Salcedo, M. Vallet-Regí and M.T. Portolés, *Biomaterials*, **30**, 45 (2009); https://doi.org/10.1016/j.biomaterials.2008.09.012
54. H. Shahoon, R. Hamedi, Z. Yadegari, V.A. Majd Hosseiny and P. Golgounnia, *J. Nanomed. Nanotechnol.*, **4**, 1000173 (2013); https://doi.org/10.4172/2157-7439.1000173
55. G. Devanand Venkatasubbu, S. Ramasamy, G.S. Avadhani, L. Palanikumar and J. Kumar, *J. Nanopart. Res.*, **14**, 819 (2012); https://doi.org/10.1007/s11051-012-0819-3
56. Z. Farooqui, M. Afsar, M. Rizwan, A.A. Khan and F. Khan, *Toxicol. Rep.*, **3**, 328 (2016); https://doi.org/10.1016/j.toxrep.2016.02.004
57. S.K. Bhavikatti, S.L.A. Zainuddin, R.B. Ramli, S.J. Nadaf, P.B. Dandge, M. Khalate and M.I. Karobari, *Sci. Rep.*, **14**, 11878 (2024); https://doi.org/10.1038/s41598-024-62915-1